Wear 556-557 (2024) 205523

Contents lists available at ScienceDirect

Wear

journal homepage: www.elsevier.com/locate/wear

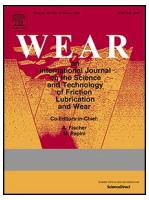

Tribocorrosion behaviour of CoCrMo in simulated body fluid under anaerobic conditions

J. Qi [a], T. Cole [a], A. Foster [b], W.M. Rainforth [a,*]

[a] Department of Material Science and Engineering, The University of Sheffield, Sheffield, S1 3JD, UK
[b] Department of Chemistry, The University of Sheffield, Sheffield, S1 3JD, UK

ARTICLE INFO

Keywords:
CoCrMo
Tribocorrosion
Anaerobic
TEM
ICP-MS
nanomegas

ABSTRACT

CoCrMo has been used as an implant material for a long time due to its excellent combination of strength, corrosion resistance and biocompatibility. The formation of a thin passive oxide film on the surface of the material plays a crucial role in its performance. This passive film can be ruptured during contact between two surfaces, but usually reforms in short timescales. However, the reformation of the film depends on the availability of oxygen in the surrounding fluid. The oxygen level in human tissue, cartilage and synovial fluid, around which the implant is situated, is much lower than that in laboratory testing under open-air conditions. Moreover, the local oxygen concentration and pH values in the body vary from patient to patient, depending on the patient's health condition and other factors, which leads to variation in the corrosion resistance of metallic implants. Therefore, an implant that performs well at one time may still experience an undesirable level of corrosion at another. Thus, evaluation of the tribocorrosion of implant materials carried out in open-air conditions does not reflect the actual process the implants undergo once in the body, particularly if there is irritation due to injury or surgery. In this study, we investigate the tribocorrosion behaviour of CoCrMo in bioactive solutions under fully aerobic to anaerobic conditions with varying loads/contact pressures. The anaerobic condition leads to a reduction in wear rate and a reduction in the extent of tribofilm formation but does not have an appreciable effect on friction. The mechanisms are discussed in detail.

1. Introduction

Cobalt-based alloys are commonly used as implant materials due to their exceptional combination of biocompatibility, wear resistance and corrosion resistance. These alloys have demonstrated excellent performance in many cases, with joint implants lasting for more than 20 years [1,2]. However, the wear particles generated can cause inflammation and tissue damage and the metal ions released can lead to adverse tissue reactions, particularly in patients with metal allergies or sensitivities [3]. The underlying reasons why CoCrMo alloys exhibit excellent performance in some cases while experiencing unacceptably high wear rates in others remain unclear [4]. However, a load-related mild-to-severe wear transition was observed for CoCrMo alloy when the applied load increased from 70N (Hertzian contact stress of 4.16 GPa) to 75N (4.26 GPa) [5]. This wear transition is closely linked to the formation of a surface nanocrystalline layer and the loss of the protective tribolayer [5].

The formation of a thin oxide film on the surface of the material is vital in preventing corrosion. This film maybe disrupted by the contacting surfaces, but in most cases it regrows rapidly. However, the formation of this oxide layer is highly dependent on the availability of oxygen in the surrounding environment. The possible electrochemical reactions occurring in this process within the current system are as follows [6,7]:

$$Cr \rightarrow Cr^{3+} + 3e^{-} \quad (1)$$

$$Co \rightarrow Co^{2+} + 2e^{-} \quad (2)$$

$$Mo \rightarrow Mo^{3+} + 3e^{-} \quad (3)$$

$$2Cr^{3+} + 2H_2O \rightarrow Cr_2O_3 + 6H^{+} \quad (4)$$

$$Mo^{3+} + 3H_2O \rightarrow MoO_3 + 6H^{+} \quad (5)$$

$$2Co^{2+} + 2H_2O \rightarrow MoO + 4H^{+} \quad (6)$$

* Corresponding author.
E-mail address: m.rainforth@sheffield.ac.uk (W.M. Rainforth).

https://doi.org/10.1016/j.wear.2024.205523
Received 11 March 2024; Received in revised form 15 July 2024; Accepted 26 July 2024
Available online 31 July 2024

However, there are significant oxygen gradients between the air we breathe (~21 kPa) and the oxygen level present in different organs and tissues (as low as ~0.5–1 kPa). For instance, human arterial blood is normally oxygenated to a level of 10–13.3 kPa (95–100 % saturation). The oxygen level at the synovial fluid around the articular cartilage and at the articular cartilage are 2.6–7.3 kPa and 1.4–1.5 kPa, respectively [8].

It has long been recognized that cell culture undertaken under room air conditions falls short of replicating the natural protection *in vivo*. However, the differences in oxygen levels between open-air conditions and the human body have not been taken into consideration when evaluating the tribocorrosion properties of implant materials. It is crucial to consider these differences when investigating the tribocorrosion behaviour of implants *in vitro*, as the electrochemistry of the media under room air conditions differs from that found in the body. Therefore, it is important to simulate appropriate oxygen levels *in vitro* to better understand the actual process the implants will undergo once in the body, especially if there is irritation due to injury or surgery.

Buckley and colleagues [9–12] have conducted extensive research on the friction and wear behaviour of various materials, including Co and Co-based alloys, under vacuum conditions. Their studies have shown that Co and Co-based materials exhibit lower friction under vacuum than in air at room temperature, with similar wear rates. Specifically, they reported that alloys with a hexagonal close-packed (HCP) structure demonstrate both low wear and low friction. However, when the temperature exceeds the phase transformation temperature, forming the FCC structure, the friction values increase four times, accompanied by a significant increase in wear by 200 times. In a related study, Cho and Lee [13] investigated the impact of oxide layers on the friction behaviour between TiN-coated balls and steel disks in air and nitrogen environments. They observed that the presence of an iron oxide layer led to a friction transition and higher friction, with the friction was lower under nitrogen compared to an air environment.

The tribocorrosion performance of CoCrMo under inert gas conditions, both with and without a solution, has not previously been studied. In this investigation, we focused on exploring the tribocorrosion behaviour of the CoCrMo alloy under aerobic, anaerobic and hypoxic conditions, where the oxygen level was deliberately maintained below 5 % saturation, specifically under high-load and high-contact pressure conditions. This research complements our previous work conducted under low-load conditions [14]. Our main goal was to examine the formation of tribofilms, evaluate the corrosion performance, and assess the wear resistance of the CoCrMo alloy in an environment characterized by extremely low oxygen content.

2. Experimental procedure

2.1. Materials and experimental set-up

A commercially available as-cast CoCrMo alloy bar, specifically designed for surgical implant applications (4.5 cm diameter, ASTM F75 specification), was used in this study. The bar was sectioned into 2 mm thick discs and a high standard polish was achieved by the standard grinding and polishing procedures [2]. In the tribocorrosion experiments, inert Al_2O_3 balls with a diameter of 5 mm (G10, 99.0 %, Atlas Ball & Bearing Co Ltd., UK) were employed as the counter-body, which is a standard approach in tribocorrosion studies.

Ultrapure water (Alfa Aesar) was used for preparation and surface cleaning/rinsing in this study. All the utrapure water utilized in these specific set of tests was pre-purged with Ar for a minimum of 40 min prior to use.

A simulated body fluid solution was created using 25 vol % Bovine Serum Albumin (BSA) (First Link Ltd., UK) in phosphate-buffered saline (PBS) (Sigma-Aldrich). This resulted in a solution with a protein content of 15.8 g/L, which falls within the normal protein content range found in the human body fluid of healthy individuals. The initial pH of the solution was 7.45 [3].

The tribocorrosion tests were conducted using a three-electrode tribocorrosion cell integrated with an EasyStat Potentiostat (Bruker, UK) on a Universal Micro Tribometer (UMT) TriboLab. The experimental setup followed ASTM G133 guidelines and utilized reciprocating sliding in a ball-on-disk configuration. The working electrode (WE) consisted of the CoCrMo coupons, while an Ag/AgCl reference electrode (RE) and a platinum wire counter electrode (CE) completed the electrochemical cell. For all tests, all samples were left for at least 30 min until the OCP stabilized. The initial OCP for all samples was stable around −0.2V. The OCPs dropped abruptly once the tribocorrosion tests started, and the data was recorded from the onset of the tests.

The stroke length used for the tests was 2 mm with a sliding speed of 0.2 m/s. The latent time (the time between two successive contact events) was 0.1 s. A total sliding time of 2 h was selected which was well into the steady state regime, which gave a total sliding distance of 1440 m. Various normal loads/contact pressures were employed in the tests, including 40N (initial Hertzian contact stress [4] of 3.0 GPa), 50N (3.2 GPa), 80N (3.7 GPa), and 90N (3.9 GPa). Each load was tested at least three times to ensure consistent results. The width in the wear scar increased with time, increasing the apparent contact area, thereby decreasing the Hertzian contact pressure. The average Hertzian contact pressure was 2.3 GPa at 40N, 2.5 GPa at 50N, 2.9 GPa at 80N and 3.0 GPa at 90N.

The tests were conducted under both aerobic and anaerobic conditions. The aerobic condition is maintained under an open-air environment without introducing additional oxygen into the system. The anaerobic condition was achieved by purging the system with Ar gas 1 h before the test and throughout the entire test duration.

The oxygen level during the procedure was monitored using an oxygen meter (HANNA HI-2004 Edge), which was calibrated before each use following the standard procedure provided by Hanna Instruments. In this calibration process, 100 % oxygen level was defined as the level near the water surface, while 0 corresponded to the oxygen level of a freshly prepared zero-oxygen solution.

For the alloy samples tested under the anaerobic condition, strict precautions were taken to maintain an Ar environment. They were extracted under Ar atmosphere, rinsed with ultra-pure water purged with Ar, and dried under Ar. Subsequently, all samples were stored under vacuum prior to conducting further post-test investigations.

2.2. Wear rate calculation

The wear volume was measured using an optical Dektak® 150 profilometer (Bruker, UK). The wear rate is then calculated by the standard formula:

$$K = \frac{V}{S}$$

Where K is the specific were rate in units of mm^3/m, V is the wear volume in mm^3, and S is the total sliding distance in m.

2.3. Characterization of the worn surface and subsurface

A FEI Helios (Nanolab G3) SEM integrated Focus Ion Beam (FIB) was used to for plan view images of the wear scar and prepare cross-sectional samples for tribolayer and subsurface analysis. A JEOL F200 transmission electron microscope (TEM) with a twin solid-state ultra-sensitive large silicon drift detectors (SDD) energy dispersive X-ray spectrometry (EDS) system operating at 200 kV was used to examine the structure and chemical composition of the interface, tribolayer, and subsurface.

The NanoMegas STAR™ precession electron diffraction (PED) and ASTAR™ automatic crystal orientation mapping (ACOM)-TEM systems, integrated with the JEOL F200 TEM, were used to acquire the phase and

crystal orientation information of the subsurface beneath the worm surface. The precession angle was 0.7°, with a precession frequency of 100 Hz and beam spot size is 10 nm. A step size of 2.5 nm for both x and y directions was used in all measurements. The diffraction patterns were collected at a camera length of 150 nm. Once collected, the dataset was matched against diffraction patterns from the database and indexed automatically by Index software (NanoMegas, Belgium). All data were exported and post-processed by the customized MATLAB scripts (originally from MTEX [15]) to calculate the grain size distribution and GND density.

2.4. Determination of ion concentrations in the lubricant and wear debris

The solution and debris were collected and subjected to centrifugation for Inductively Coupled Plasma Mass Spectrometry (ICP-MS) analysis to quantify the concentrations of dissolved ions in the lubricant solutions and the wear debris generated during the testing processes, respectively.

2.4.1. Sample preparation for ICP-MS

Following tribocorrosion testing, lubricants were transferred to Argon-pre-purged 50 ml Millipore Amicon® Ultra-15 centrifugal tubes in a well-controlled air-free environment for the separation of wear debris and solutions. These tubes consist of a filter tube for collecting particles and large molecules, and a solution tube for the filtered solution. Debris and solution separation was achieved by centrifugation at 4700 rpm using two different filter sizes: 100,000 for 30 min and 30,000 for 10 min. This ensured that particles smaller than 100 nm remained in the filter. The process was repeated multiple times, and debris and solutions from the same sample were collected separately. Debris was then

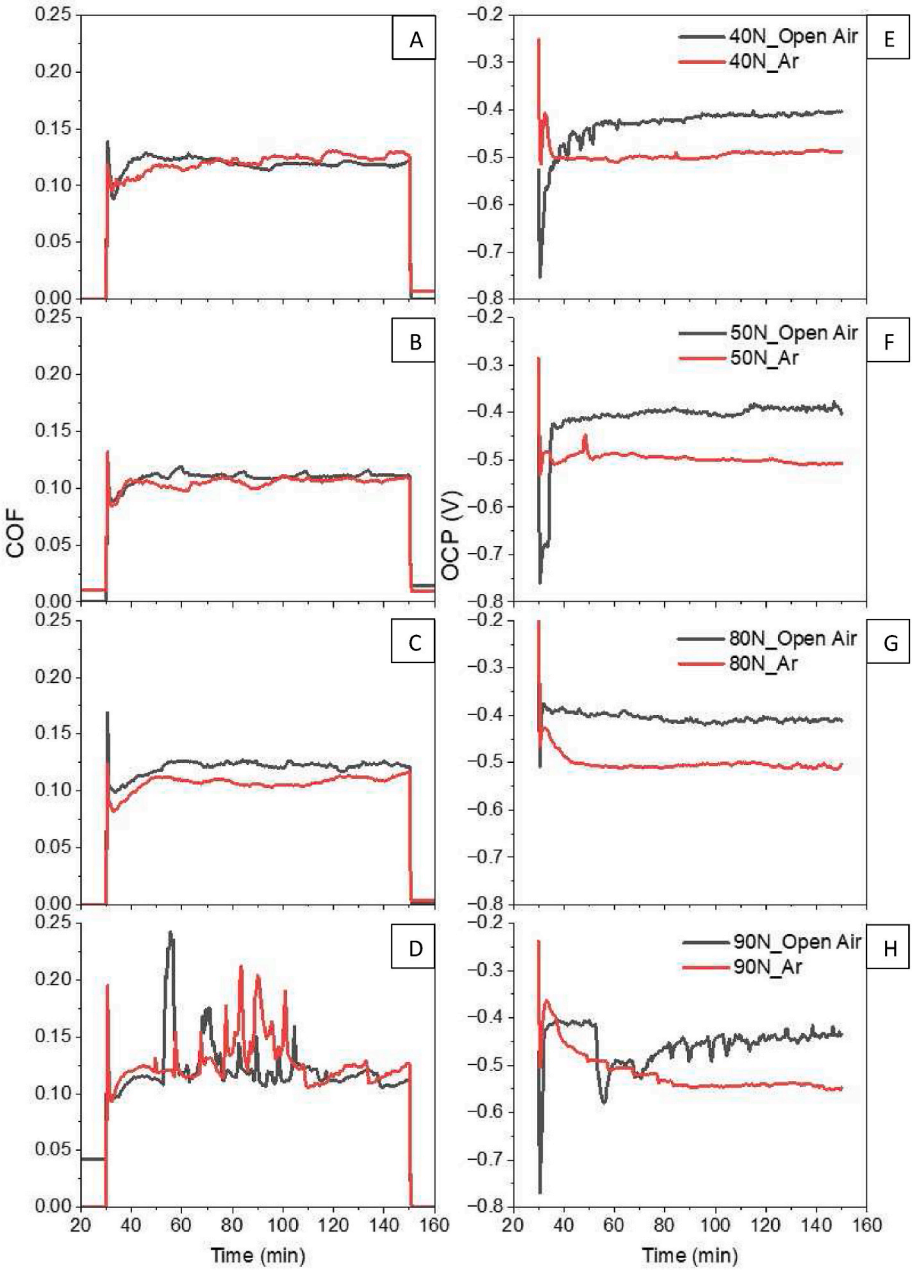

Fig. 1. COFs (left panel, A: 40N, B: 50N, C: 80N, D: 90N) and OCPs (right panel, E: 40N, F: 50N, G: 80N, H: 90N) results from tests under different loads. The red line represents the test carried under Ar and black lines refer to the ones from open-air. (For interpretation of the references to colour in this figure legend, the reader is referred to the Web version of this article.)

dried under argon, and all samples were stored in a freezer prior to ICP testing.

2.4.2. ICP-MS analysis procedure

ICP-MS analysis was performed using an Agilent 7500ce ICP-MS. The instrument was calibrated prior to analysis using commercially available standards (SPEX CertiPrep, Fisher Scientific and TraceCERT, Sigma Aldrich). Elements were measured using isotopes Cr 53, Co 59 and Mo 95. Yttrium was used as an internal standard. Solution samples were diluted 100-fold with 1 % nitric acid prior to measurement. Dried wear debris were transferred to pre-weighed 50 ml glass tubes, followed by the addition of concentrated nitric acid and digestion at 170 °C for 30 min. The resulting digest was then centrifuged, and the supernatants were analysed using the same method as the solutions. Results are reported in μg/kg based on weight.

3. Results

3.1. Tribocorrosion results

Fig. 1 presents the coefficient of friction (COF), left panel, and open-circuit potentials (OCPs), right panel, of the tests conducted under different loads, both in open-air and Ar environments. The red line indicates the tests from the Ar condition and the black lines refer to the open-air condition. The COFs exhibit only small variations across all loads for both testing environments, except for the 90N load (Fig. 1D), where the COFs in both Ar and open-air conditions appear much noisier compared to other loads. This reflects the rapid changes in surface conditions caused by the high load.

In the open-air condition, the OCPs initially reach a low point of approximately −0.75V, except at 80N (Fig. 1G), where it only reaches −0.5V, and they then rise quickly and stabilize around −0.4V. At 90N (Fig. 1H), the OCP initially stabilizes around −0.4V, then drops to −0.6V before rising again and fluctuating around −0.45V. In contrast, the OCPs in the Ar conditions drop to around −0.5V, then rise slightly after the running-in period, and remain stable around −0.5V in most cases, except the 90N test, where the OCP drifts down to −0.6V. Overall, the potentials obtained in the Ar conditions are lower than those in the open-air conditions, indicating the difference in passivation of the surface.

3.2. Wear rate

Fig. 2 shows the wear rate evaluated in tests conducted under both Ar (red diamonds) and open-air (blue diamonds) conditions, with the upper x-axis representing the calculated initial contact pressure and the lower x-axis giving the applied loads. The results consistently show that the wear rate is higher in the open-air condition compared to the Ar condition, regardless of the applied load. Moreover, as the load or contact pressures increase, the difference in wear rate between the two conditions becomes more prominent. Notably, a wear-transition occurs between 80N and 90N in both the Ar and open-air environments. At 90N, the wear rate in the open-air condition exceeds that at 40N by more than 10-fold. Similarly, the wear rate of the samples tested under Ar at 90N is approximately 8 times higher than that at 40N.

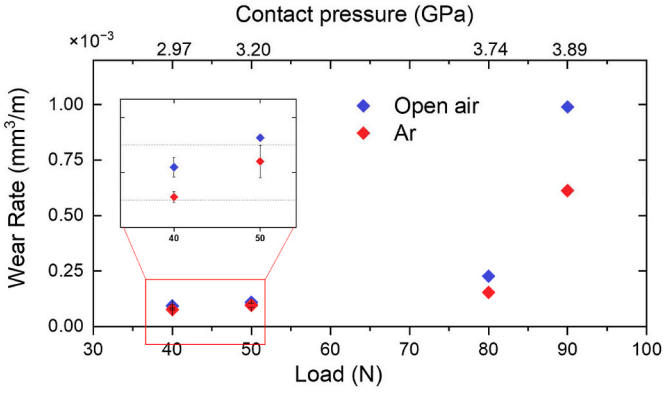

Fig. 2. Comparison of wear rate of tests carried out under open-air (blue diamond) and Ar (red diamond) at various loads/contact pressures. The inset is the enlarged diagram of the red box. (For interpretation of the references to colour in this figure legend, the reader is referred to the Web version of this article.)

3.3. Surface morphology after tribocorrosion tests

Fig. 3 presents plan view SEM images of the wear track from the 40N and 90N tests, under both Ar and open-air conditions. The top panel displays four images positioned above the red line, representing the Ar condition, while the bottom panel exhibits four images positioned below the red line, representing the open-air condition. The left column corresponds to the samples tested at 40N, whereas the right column gives samples tested at 90N. Additionally, Fig. 1B–D, F, and H are enlarged images that provide detailed views of the wear track.

In general, the wear tracks observed in the samples subjected to a load of 40N appear clean and smooth, regardless of the testing environments (Ar or open-air). However, in contrast, the wear tracks at 90N show noticeable signs of ploughing and the presence of wear debris (Fig. 1F and H). Furthermore, it is important to note that the surfaces exposed to open-air conditions exhibit rougher textures compared to those tested under Ar conditions. The sample tested under 40N in open-air (Fig. 1D) shows a greater amount of wear debris compared to the corresponding sample in Ar (Fig. 1B). Moreover, the wear track of the sample tested under 90N in open-air (Fig. 1H) exhibits deep ploughing and surface damage, while the corresponding sample in Ar only displays mild ploughing and noticeable amount of wear debris.

3.4. Tribofilm and subsurface structure

To reveal of the nature of the tribofilm on the top surface and the microstructure of the subsurface underneath it, four FIB samples were taken on the centre of the wear tracks along the sliding direction from both Ar and open-air condition for the 40N and 90N tests. Fig. 4 presents the microstructure of the subsurface and the tribolayer for both open-air and Ar samples under a 40N load. Fig. 4A and B give scanning transmission electron microscopy (STEM) high-angle annular dark field (HAADF) images, highlighting surface modifications and damage after the tests. To safeguard against potential damage during the process, a layer of platinum (Pt) was deposited on the wear track surface prior to FIB sample preparation.

In the open-air sample, beneath the Pt deposition, a region with dark contrast on the outer surface is wear debris, labelled in Fig. 4A. Below the debris, a relatively uniform layer with greyish contrast was observed. Careful observation shows a thin layer, exhibiting dark contrast, between the Pt deposition and the grey layer. This dark layer, measuring approximately 60 nm, comprised an amorphous structure embedded with some nanoparticles, as shown in Fig. 4C. Previous studies [16–18] have revealed that both layers are tribo-layers, exhibiting distinct chemical compositions and microstructures, as discussed in the following section. A heavily deformed nanostructured region was observed between the tribolayer and the substrate, which preserved the original grain microstructure of the CoCrMo material, although it contained more deformation twins and martensite plates than in the starting material. The grains within this nanostructured region exhibited noticeable bending along the sliding direction.

No surface debris was observed in FIB sections of the Ar sample, Fig. 4C and D. A thin layer with grey contrast was observed beneath the Pt deposition. Fig. 4D provides detailed images of this layer, which exhibited an amorphous structure and had a thickness of approximately 20 nm. In comparison to the similar layer on the open-air sample, this

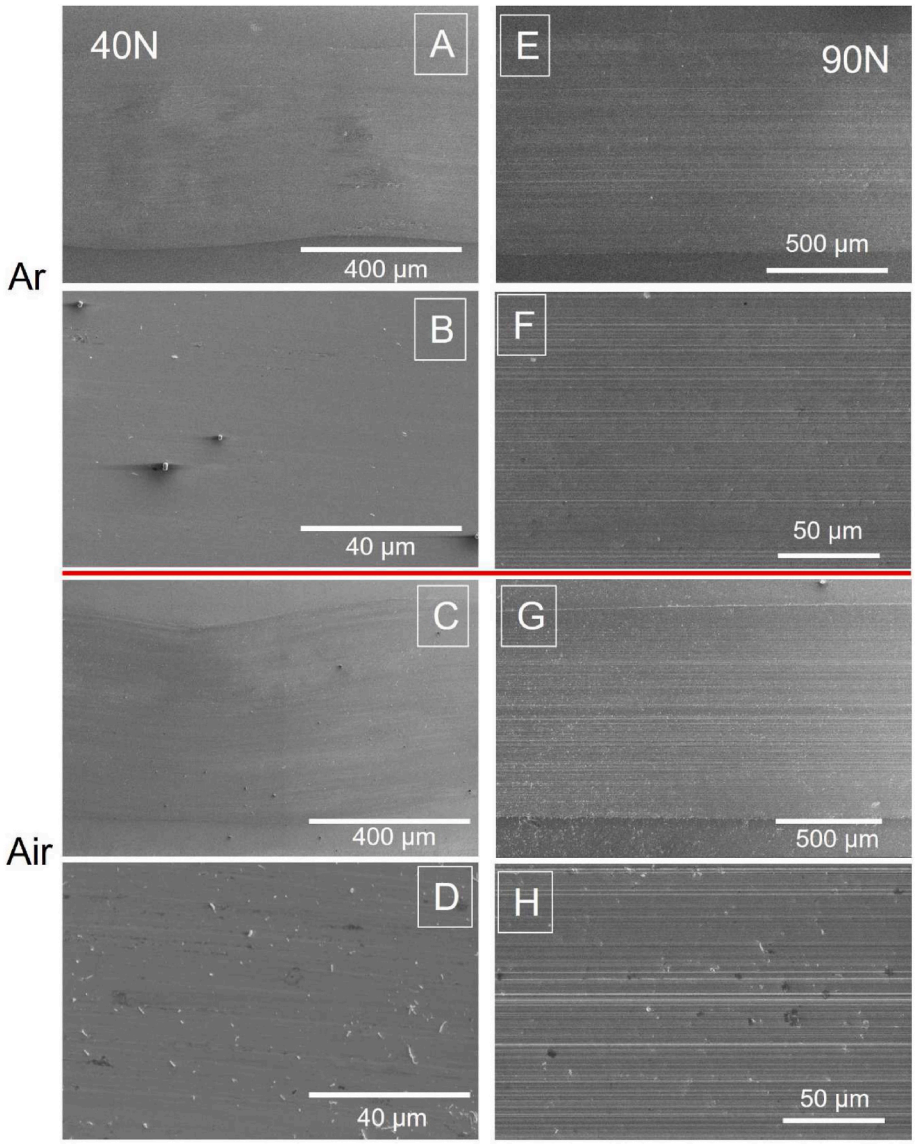

Fig. 3. SEM images at various magnification show wear tracks morphology of samples tested under 40N (A, B, C, D) and 90N (E, F, G, H) from Ar and open-air conditions. The left column is 40N and the right one is 90N. The panel above the red line is under Ar and below the red line is under open-air. (For interpretation of the references to colour in this figure legend, the reader is referred to the Web version of this article.)

layer was thinner and less uniform. Importantly, no thick tribolayer (such as the one seen on the open-air sample with grey contrast in Fib.4A) was present on the Ar sample. A nanocrystalline layer was observed between the tribolayer and the low strain substrate that largely retained its original structure. However, the grain size within this nanocrystalline layer in the Ar sample was significantly larger than that in the open-air sample, which will be discussed further in subsequent sections. Minimal grain bending was observed along the sliding direction in the Ar sample. It is also noteworthy that the top surface layer of the open-air sample is uniformly level across the entire sample, while the top surface of the Ar sample exhibits unevenness at this magnification scale. Careful observation reveals that the metal substrate below the tribolayer in the open-air sample is also rough, but the worn surface itself appears level due to the presence of the tribolayer.

A tribofilm is present, ~160 nm thick, for the open-air samples tested at a load 90N, which appears to have a two-phase structure as shown in the enlarged image in Fig. 4F. While the thickness of the tribolayer for the sample tested under 90N Ar condition is only about half of the one under open-air condition, which is 80 nm. The tribolayer from the open-air at 90N contains numerous nanoparticles, with much less amorphous material embedded. This structure is very different to the ones from both 40N samples and sample from 90N Ar condition. In addition, cracks and openings are also only observed at the tribolayer of the 90N open-air sample as indicated by the red stars in Fig. 4E.

Fig. 5 shows EDS maps of the surface regions of the open-air and Ar samples tested at 40N and 90N. The open-air sample under 40N includes a wear debris particle (dark contrast on the surface). Underneath this, a multi-layered tribofilm structure was observed, consisting of a layer showing grey contrast, followed by a layer with darker contrast, indicated by the white and red arrows, respectively. The region below these layers corresponds to the nanocrystalline region. The EDS maps shows that the wear debris particle is a mixture of carbon- and oxygen-rich compounds, with some embedded Cr and Co oxide particles. The topmost grey amorphous tribofilm, located directly below the wear debris, is predominantly composed of Co and Mo, with a small amount of Cr, but with no oxygen. The dark, thin layer is most likely composed of Cr oxide.

In contrast, the composition and structure of the tribofilm on the Ar sample tested at 40N are relatively simpler. The light grey layer primarily consists of a carbon-rich thin layer, likely formed through tribo-

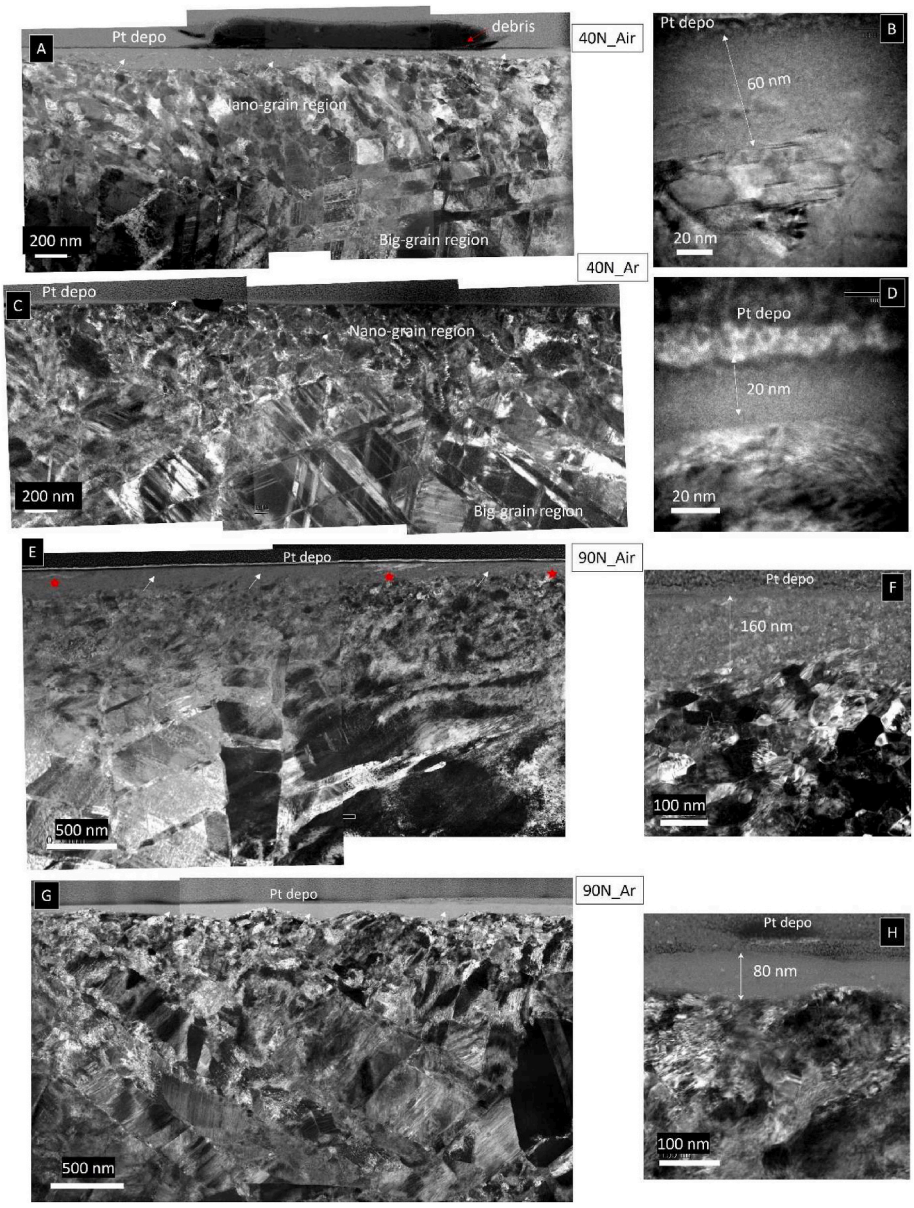

Fig. 4. STEM ADF images show the subsurface of the CoCrMo after the tribocorrosion tests at 40N and 90N loads, for A and B) 40N in the open-air, C and D) 40N under Ar, E and F) 90N in the open-air, and G and H) 90N under Ar. Wear debris is highlighted by a red arrow in A, and the tribolayer is indicated by white arrows. B, D, F and H are the high-resolution images that provide detailed views of the tribolayer on the topmost surface for the open-air and Ar samples. The red stars in E indicate the cracks and openings on the tribofilm. (For interpretation of the references to colour in this figure legend, the reader is referred to the Web version of this article.)

induced reactions with proteins in the solution acting as precursors. Minimal oxygen was detected, approximately at background levels. This confirms that there is no oxide layer formed on the surface.

For the samples tested at 90N, the tribolayer on the open-air samples is rich in O and Mo, with a slight enrichment in Co. The Cr was heterogeneously distributed, with Cr rich regions depleted in Mo and Co, while Cr depleted regions were rich in Co and Mo. In contrast, the tribolayer on the Ar sample, which is much thinner than the open-air sample, is O and Cr free, but is enriched in Mo and C, with some enrichment of Co. The detailed analysis of the elemental ratios for the tribolayers and bulk materials for all samples presented here will be discussed in section 5.

Precession Electron Diffraction (PED) was undertaken on FIB cross sections of the surface to characterize the microstructural deformation of the subsurface regions following the tribocorrosion tests at 40N and 90N in both Ar and open-air environments. The results are shown in Fig. 6. The 1st and 3rd panel in Fig. 6 represents the results obtained from the sample tested under open-air conditions for 40N and 90N, respectively. While the 2nd and 4th panel corresponds to the sample tested under Ar for 40N and 90N, respectively. Fig. 6A, D, 6G and 6J display bright-field (BF) images, indicating the positions of the selected sites on the cross-sectional samples. Importantly, all samples originate from the same commercially available CoCrMo alloy, meaning identical initial phases and microstructure. However, Fig. 6 clearly demonstrates that the microstructures and phases of the final materials differ significantly.

Analysis of the grain boundary, orientation, and phase maps reveals that the samples tested under Ar (Fig. 6F and L) exhibit larger grains and a reduced quantity of grains in the nanocrystalline region, as indicated by the white dash-dot lines, compared with their corresponding counterparts tested under open-air (Fig. 6C and L). Grain bending, serving as the indicator of surface strain and denoted as the schematic drawing in Fig. 6B, E, 6H and 6K, is more noticeable in the 40N and 90N open-air

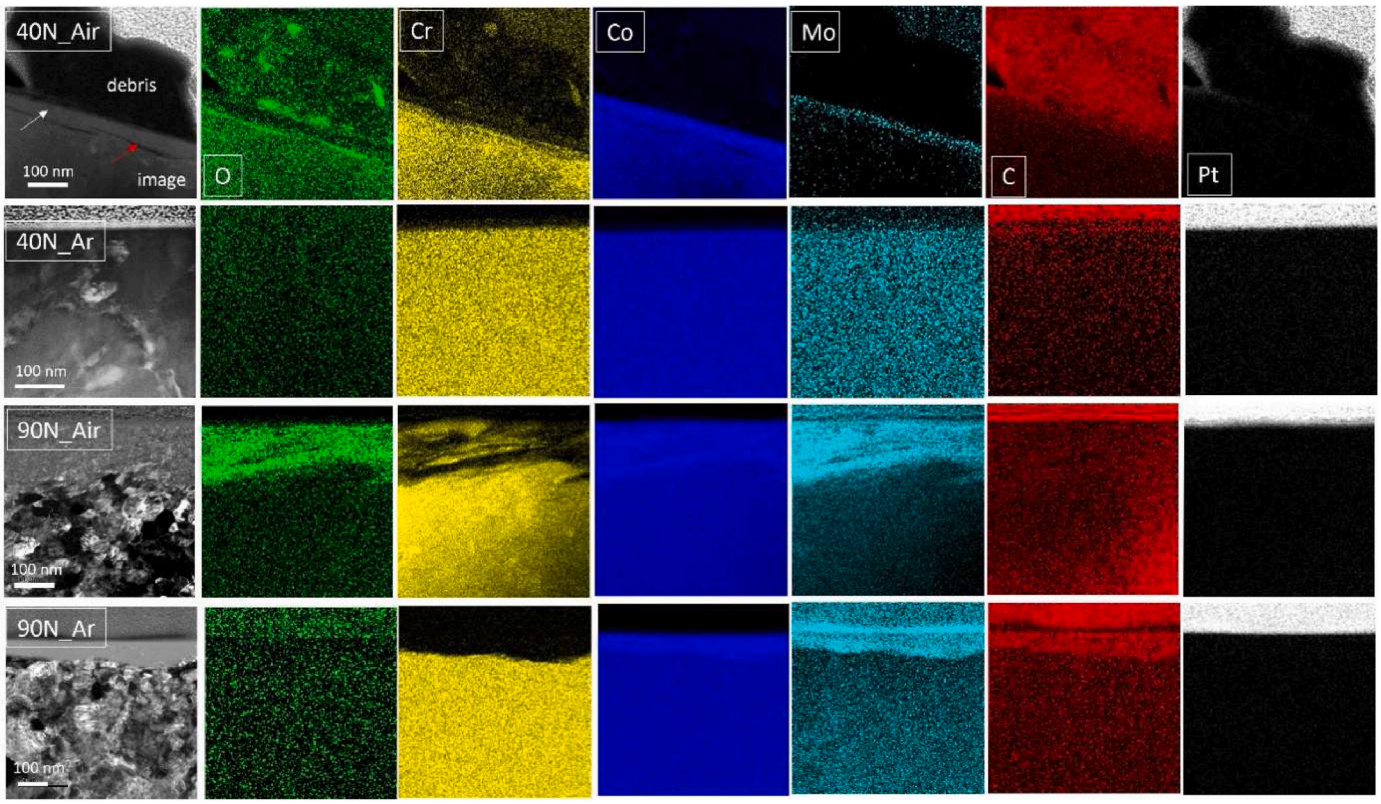

Fig. 5. STEM/EDS maps show the elemental distribution in the tribolayer and subsurface of samples tested under 40N and 90N. The 1st and 3rd panels are for the open-air samples and the 2nd and 4th panels are taken for Ar samples.

samples (1st and 3rd panels) but less prominent in the Ar samples (2nd and 4th panels).

The starting material was predominantly composed of the FCC (face-centered cubic) phase. However, under the 40N test conditions, sliding-induced phase transformations occurred, leading to the conversion of the FCC phase to the HCP (hexagonal close-packed) phase, which is the thermodynamically stable phase at temperatures below 500 °C. Interestingly, a higher percentage of FCC-to-HCP phase transformation was observed in the open-air environment, with a fraction percentage of 82.3 % in the final material, compared to 73.6 % in the sample tested under Ar. Thus, extensive friction induced phase transformation had occurred, particularly in the nanocrystalline region. In contrast, the less deformed region closer to the bulk material retains a higher proportion of the original FCC phase. This is a result from the lower level of mechanical deformation in this region, along with reduced shear forces.

The transformation was more pronounced in the 90N tests than the 40N tests, with significant extension into the bulk material from the nanocrystalline region beneath the worn surface. Notably, in the 90N tests, the heavily deformed layer's depth was greater in the Ar sample (~1.4 μm) than in the open-air sample (~700 nm). However, the size of the nanocrystals was much smaller in the open-air sample compared to the Ar sample. Fig. 6I and L give phase maps, again of the same areas. The majority of the structure has transformed from FCC to HCP, with similar volume percentage levels in both samples (open-air test: 10.9 % FCC and 89.1 % HCP and the Ar test: 9.1 % FCC, 90.9 % HCP).

To further analyse the deformation and potential damage resulting from the tests, the geometrically necessary dislocation (GND) density was computed based on the acquired precession electron diffraction data. GNDs are dislocations with a consistent Burgers vector sign that accommodate plastic strain gradients within the microstructure. The GND was separately determined for each phase, and for the HCP phase, the GNDs were additionally mapped for the prismatic and basal slip systems. The calculated GND density distributions for both the Ar and open-air samples subjected to 40N and 90N loads are given in Fig. 7. They are the same regions that were examined in Fig. 6.

The dislocation density in the FCC phase was similar for all the samples with very little strain accommodated in the FCC structure. In contrast, the HCP phase exhibited a significantly greater dislocation density. The basal slip system exhibited a significantly higher dislocation density compared to the prismatic slip system, which is expected. The dislocation density was found to be higher in the nanocrystalline regions for all samples. All samples exhibited clusters of high dislocation density concentrated near the boundary between the nanocrystalline region and the large-grain region. Additionally, the HCP phase exhibited a significantly greater dislocation density compared to the FCC phase, primarily due to its dominance near the surface. Furthermore, within the HCP phase, the basal slip system displayed a notably higher dislocation density compared to other slip systems.

When comparing the two test conditions, the dislocation density in the FCC phase was similar. However, in the HCP phase, both the basal and prismatic slip systems exhibited a higher dislocation density in the sample tested under open-air conditions compared to the sample tested under Ar conditions. Notably, the sample tested under open-air contained a greater number of high dislocation density clusters on its surface compared to the sample tested under Ar. Both samples exhibited clusters of high dislocation density concentrated near the boundary between the nanocrystalline region and the large-grain region.

3.5. Ion concentration in test solution and wear debris

Fig. 8 present the ICP-MS concentrations in μg/L of the Cr, Co and Mo in the debris and post-test lubricant solutions and Table 1 summarises the ratios of the elements. The ratio of the elements in the initial starting material is Co:Cr: Mo = 64.9: 27.5: 5.3 in weight%, which is also listed in Table 1. As expected, in both the wear debris and the solution, the concentrations of Cr, Co, and Mo increase with increasing load for all

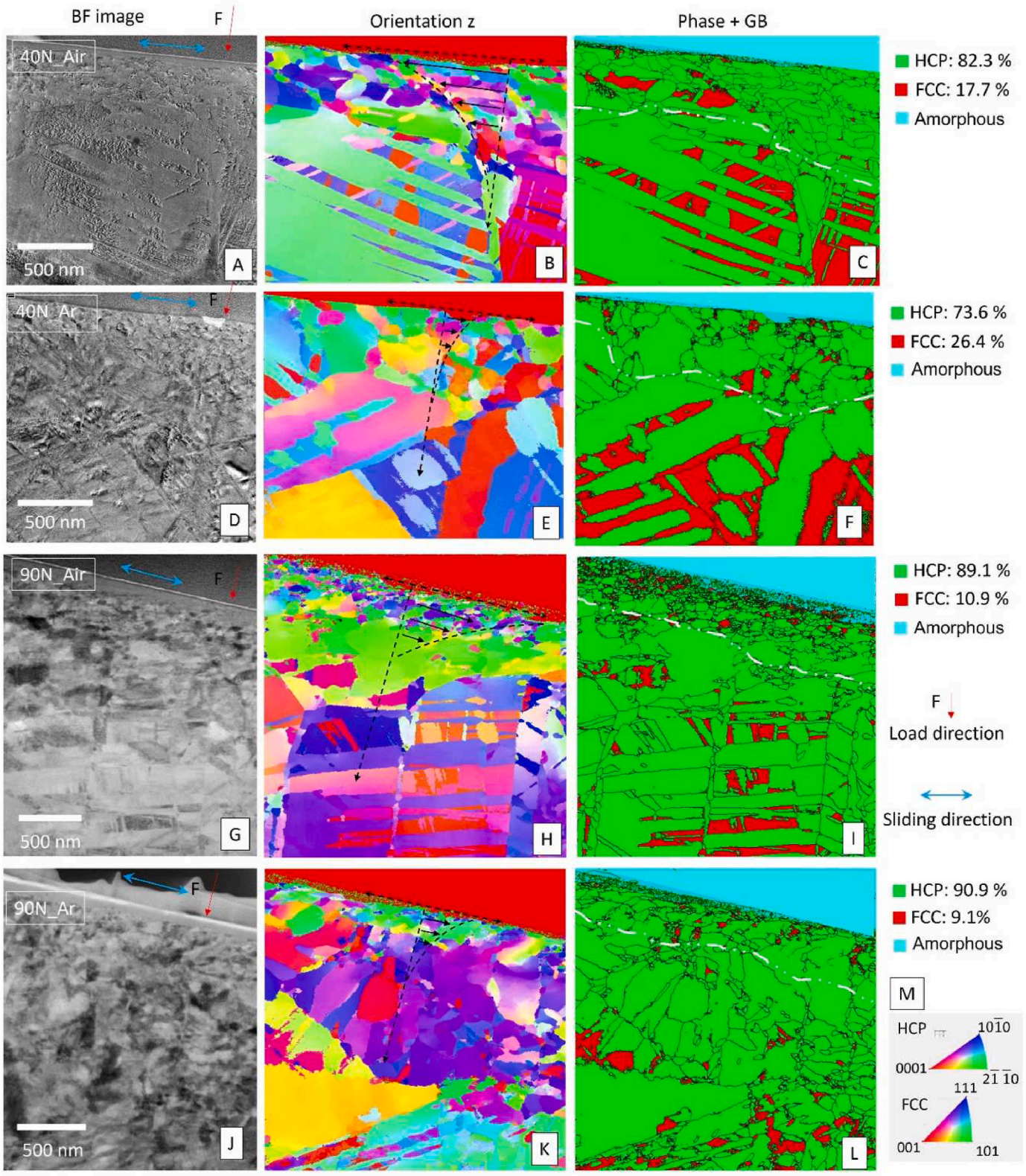

Fig. 6. NanoMegas results for Ar and open-air samples under 40N (A to F) and 90N (G to L) load. The top and 3rd panels (A to C, and G to I, respectively) shows BF images and corresponding crystallographic z-orientation, and phase maps super-imposed with grain boundary, for the open-air samples. The 2nd and 4th panels (D to F, and J to L, respectively) presents the same maps for the Ar samples. The colour keys for z-orientation maps are provided (M). The percentage fractions of measured phases are presented next to the phase maps (C, F, I and L), where green is HCP, red is FCC and cyan is amorphous. The blue double arrows indicate the sliding direction and surface position, while the red arrows represent the applied load direction. Schematic drawings in B, E, H and K illustrate the strain distribution from the surface to the bulk material. (For interpretation of the references to colour in this figure legend, the reader is referred to the Web version of this article.)

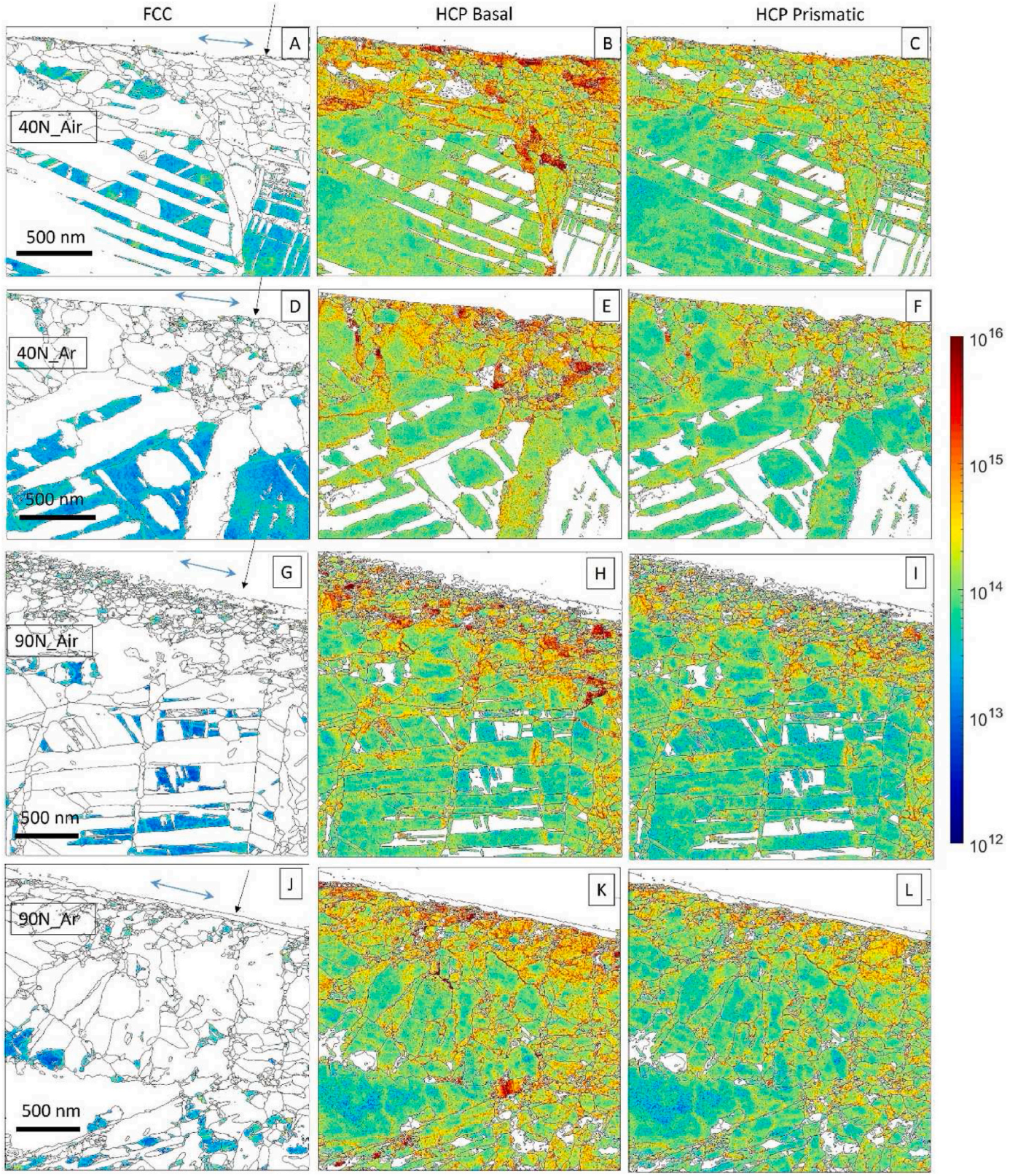

Fig. 7. Geometrically necessary dislocation (GND) distribution maps of FCC, HCP basal and prismatic slip systems for samples tested under 40N and 90N in open-air (top panel, A to C and 3rd panel, G to I) and Ar (2nd panel, D to F and 4th panel, J to L) environments. The colour scale is log(GND density in m^2). The blue double arrows denote the sliding direction and surface position, while the black arrows represent the direction of the applied load, which is towards the sample and normal to the surface and sliding direction. (For interpretation of the references to colour in this figure legend, the reader is referred to the Web version of this article.)

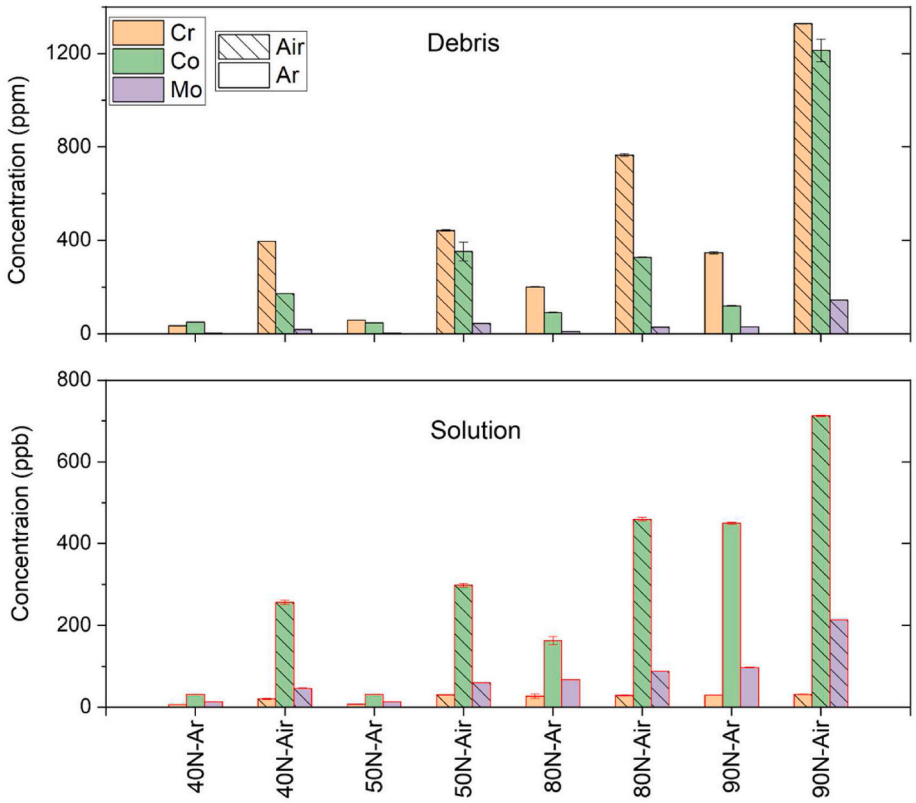

Fig. 8. ICP-MS elemental analysis for Co, Cr and Mo of the wear debris (top with black border) and lubricant solutions (bottom with red border) from the open-air samples (shaded) and Ar samples (blank) across the tested loads. (For interpretation of the references to colour in this figure legend, the reader is referred to the Web version of this article.)

Table 1
Ion concentration ratios in weight % of the wear debris (top) and post-test lubricant solutions (bottom) for all samples across the tested loads.

Debris Load (N)	Open-air: Co:Cr:Mo (%)	Ar: Co:Cr:Mo (%)
40	29.3 67.8 2.9	58.4 40.1 1.5
50	18.8 77.3 3.9	43.6 54.6 1.8
80	29.2 68.3 2.5	30.2 66.9 2.9
90	45.2 49.4 5.4	24.0 70.0 6.0
Initial bulk material	64.9 27.5 5.3	
Solution Load (N)	Open-air: Co:Cr:Mo (%)	Ar: Co:Cr:Mo (%)
40	80.7 5.6 13.7	62.6 12.3 25.1
50	76.7 7.9 15.4	61.4 13.5 25.1
80	79.9 4.9 15.2	63.4 10.6 26.0
90	74.4 3.3 22.3	78.1 5.1 16.8
Initial bulk material	64.9 27.5 5.3	

samples tested in both open-air and Ar environments. The samples tested in Ar consistently exhibit lower concentrations than their open-air counterparts both in the wear debris and the solution, aligning with the wear rate data (Fig. 2).

The ratio of the elements in the wear debris and the post-test solution are quite different to that in the starting material. In the wear debris, the concentration of Cr is much higher than in the starting material for both open-air and Ar tests. In contrast, in the post test solution, the Cr content is lower than in the starting material, for both open-air and Ar tests. Moreover, the Mo content in the post-test lubricant solution is significantly higher than in the initial CoCrMo material for all tests.

The Mo content was lower in the wear debris from the Ar tests compared to the open-air tests for all loads. Generally, the Cr content was higher in the wear debris from the open-air tests compared to those in Ar, except at 90N, where the Cr content was higher in the Ar test. The Cr content was significantly lower in the solution samples from the open-air test compared to the Ar test, while the Mo content was significantly higher in the Ar tests compared to the open-air samples. The low Cr content in the solution is consistent with the lower Cr detected at the worn surface by EDX, as shown in Fig. 5. This suggests selective removal of the surface material as wear debris.

4. Discussion

The results clearly establish the substantial impact of the oxygen level in the solution on the tribocorrosion behaviour of the CoCrMo alloy across the load range tested here. In the open-air condition, the solution's oxygen level ranged from 80 % to 100 %, while under Ar conditions, the solution's oxygen level was effectively maintained below 5 % by controlling the flow rate of Ar gas.

The COF exhibited minimal variation across the load range, except at 90N where the COF exhibited significant variations for both conditions, which coincided with a rougher worn surface (Fig. 1). At 80 and 90N, the friction was marginally higher for the open-air compared to the Ar condition. SEM images of the 90N wear track showed substantially greater grooving for the open-air compared to the Ar condition (Fig. 3D and H), which is consistent with the higher friction in the former. In addition, the FIB experiments showed a greater level of deformation at the worn surface for the open-air condition compared to the Ar tests (as discussed in more detail later), suggesting that the deformation component of the friction coefficient, μ_{def}, was higher for the open-air tests, consistent with the higher observed friction.

The OCP for the Ar condition did not vary as a function of load, within statistical variation. This is consistent with the absence of a passive film throughout the load range. The OCP for the air condition exhibited a marginal rise between 30 and 40N, with 80N similar to 40N, followed by a drop at 90N. The mean OCPs were lower (more negative) in the Ar condition compared to the open-air condition (Fig. 1),

indicating the presence of a passivation layer on the sample surface in the open-air condition, but its absence under Ar. This observation is supported by the detailed FIB/TEM results where EDS of the outer worn surface (Fig. 5) clearly shows the presence of an oxide layer on the surface of the sample from the open-air environment, while no oxide was present on the sample from the Ar condition. It was not just the oxide that was present, but also an amorphous tribolayer that was much thicker on the open-air condition than for the Ar. It is known that such layers can be passivating in the same way as an oxide [16]. Thus, the microstructural observations of surface oxide and tribofilm are completely consistent with the OCP results.

The detailed TEM investigations showed important differences between the worn surfaces of the open-air and Ar tests, Figs. 4–7. The differences fell in three categories: the presence of an oxygen-rich layer, the extent of tribofilm formation and the strain accumulation in the metal. As the TEM analysis of the samples from the 40N and 90N tests show, the worn surface of the open-air tests exhibited an oxygen-rich layer at both 40N and 90N, as expected and consistent with earlier results [16–18]. This layer was thin (~20 nm) on the 40N test and largely consisted of Cr and O. At 90N the oxygen-rich layer was thicker (~160 nm), and quite heterogeneously distributed on the surface with a more complex mixture of oxides. In contrast, no oxide was present on the worn surface of the Ar tests at 40 and 90N, which is consistent with the starvation of oxygen in the lubricant. This is similar to the surface condition under cathodic conditions, as shown by Ref. [17]. In addition, a tribolayer was observed on all samples, which was much more extensive for the open-air condition compared to the Ar tests, Figs. 4–7. For both test environments and loads, the tribolayer had a largely amorphous structure, composed mainly of Co and Mo, with some C and was depleted in Cr. For the Ar test at 40N, the tribolayer was just 20 nm thick and covered much of the worn surface in a relatively uniform manner. It was thicker at 90N (~80 nm), but still quite uniform in surface coverage. In contrast, for the open-air tests at 40N the tribolayer varied in thickness from ~60 nm to ~200 nm, while at 90N it was intermixed with the oxides in a heterogeneous manner, embedded with a large number of nanoparticles. The multilayer tribofilm structure is similar to that observed on the worn surface of Ti–6Al–4V tested under similar (OCP) conditions [16], which was strongly related to the presence of protein in the lubricant.

Given the limited availability of data in the literature on tests conducted under anaerobic conditions similar to those reported in this study, the most appropriate analogy to highlight the distinctions between the open-air tests and tests conducted in Ar is to compare the present results with those involving potential changes from cathodic to anodic. In this context, the findings on the effect of potential indicate that the tribolayer, as distinct from the oxide layer, becomes thinner as the potential is reduced, changing from relatively thick under anodic conditions to only a few nm under cathodic conditions [16]. In this case, it is appropriate to compare the Ar tests in the current work with cathodic conditions for a passivating metal in Ref. [16].

The third difference between open-air and Ar tests was the extent of deformation at the worn surface. In comparison to the Ar test, the worn surface from the open-air test at 40N exhibited a greater depth of deformation, a finer nanocrystalline grain size, greater transformation from FCC to HCP (which is strain induced) and a higher density of geometrically necessary dislocations (GNDs). For the 90N test, the open-air sample exhibited a much finer nanocrystalline structure than the Ar test, and a greater transformation from FCC to HCP, indicating a higher surface strain.

The principal variable affecting the strain accumulation is the stress field that is acting at the surface. However, the same load was used here for each condition and given that the friction coefficient observed was similar, the stress field must have been similar in each case, and therefore this factor cannot explain the differences in strain accumulation observed in Figs. 4–7. The only remaining difference between the two conditions was the presence of an oxide and the thicker tribofilm on the open-air sample compared to the Ar test sample. In the current study the main difference between the open-air and the Ar tests was the presence of an oxide in the former and its absence in the latter. This difference therefore replicates the differences between cathodic and anodic conditions, as investigated by Perrett et al. [19]. Perret et al. [19] looked at an austenitic stainless steel and found that the depth of deformation was strongly affected by the polarisation; under cathodic conditions, with no oxide present, the formation of a nanocrystalline layer was minimal, while under anodic conditions the nanocrystalline layer extended up to 10x the depth as that found under cathodic conditions. Similar observations were made by Favero et al. [20] and Bidiville et al. [21]. Perret et al. [19] suggested that the difference in strain accumulation was associated with the ease with which dislocations can be lost from the surface; the presence of an oxide in the anodic case is believed to block the annihilation of dislocations at the surface, leading to extensive strain accumulation, while under cathodic conditions, dislocation annihilation could occur at a free metal surface. It seems remarkable that an oxide film that is only a few nm thick can result in such large difference in strain accumulation, with deformation extending several tens of microns below the worn surface where an oxide is present. While remarkable, the absence of any other viable explanation indicates that this is true and that the strain accumulated in the current work depends on the presence or absence of an oxide controlling dislocation annihilation at the surface, in just the same way that found under cathodic and anodic conditions by Perret et al. [19].

The wear rate of the open-air condition was consistently higher than the Ar tests, irrespective of the tested load (Fig. 2). The wear under Ar conditions must be dominated by mechanical wear as the absence of oxygen will have prevented wear activated corrosion. In contrast, the wear in the open-air conditions will have had a measurable wear activated corrosion. This result is similar to that of Perret et al. [19] who found a near tenfold increase in wear rate in going from cathodic to passive potential, which must be associated with the wear activated corrosion. Again, the current results compare well with studies of the effect of applied potential on the wear behaviour of this material. In the current tests the wear debris on the samples from the open-air condition were predominantly carbon-based, but also contained some Cr-based oxides. Thus, the wear debris had formed by a removal of both the tribofilm and the surface oxide layer, but not from the metal substrate, consistent with corrosion-enhanced wear.

Major differences were observed in the composition of the wear debris and the lubricating solution and in both of these to the Co:Cr:Mo content of the starting material. The Cr content in the wear debris was far higher than in the starting material, while the Mo level was lower, except the 90N test, Fig. 8, Table 1. In contrast, in the post-test solution, the Cr content was well below that in the starting material, while the Mo content was much higher. It is well-established that chromium and chromium oxides exhibit lower solubility in the lubricating fluid compared to cobalt and molybdenum, and their respective oxides, while molybdenum oxides are relataively more soluble [22–24]. Simoes et al. [25] investigated wear debris particles and their dissolution following testing of metal-on-metal CoCrMo couples in a hip simulator, with the results compared to wear debris generated by milling CoCrMo powders. They found that Mo dissolution was enhanced by the presence of bovine serum albumin (BSA), which they suggested was due to the formation of metal protein complexes. Thus, the observation here of enhanced Mo content in the post-test solution is entirely consistent with the work of Simoes et al. [25].

To investigate this further, we conducted detailed elemental analysis of the worn surfaces using EDX in the TEM. The same set of samples shown in Fig. 5 were employed, with approximately 50 sites selected for point analysis in both the tribolayer and bulk material. The results, specifically focusing on the Co:Cr and Mo content ratios (wt.%), are plotted in Fig. 9A and B. The ratios of Co:Cr and Mo content in the bulk material are consistent with the initial starting material. However, in the tribolayer, the ratios exhibited a wide range, indicating an uneven

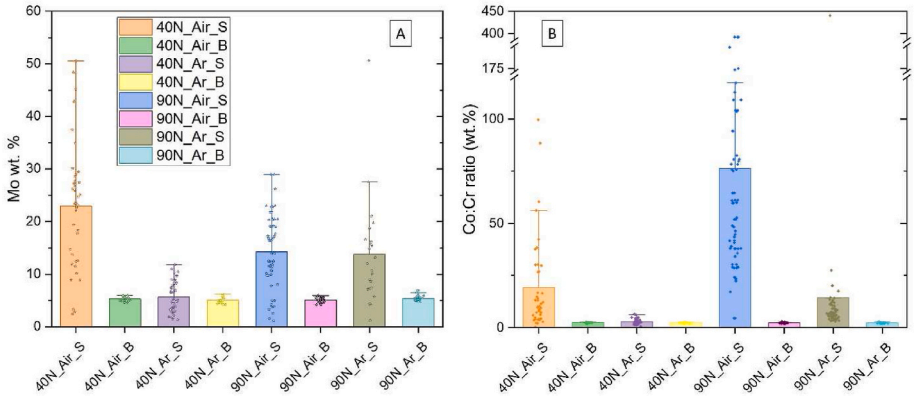

Fig. 9. STEM/EDX point analysis results of A) Mo content (wt. %) and B) Co: Cr ratio (wt. %) on the top surfaces and the bulk (B stands for bulk and S stands for surface).

distribution of elements across the worn surface, consistent with the findings from ICP-MS analysis. The sample tested at 40N under Ar exhibited the smallest range among all samples. The Mo content was enhanced in the surface the most in the open-air test at 40N, followed by the open-air test at 90N, although the Mo levels in this case were similar those observed for the Ar test at 90N. This suggests that the Mo is rejected from the oxide as it forms in the open-air tests, consistent with the low Mo levels in the wear debris, Table 1. The Cr levels in surface tended to be depleted in the open-air tests, which is consistent with the formation of a chromium based oxide which forms the wear debris.

The role of the starting microstructure on the contributions of mechanical and chemical wear mechanisms was analysed in detailed by Namus et al. [26], who looked at the tribocorrosion of CoCrMo alloys with the same starting microstructure as used here, but also utilising the same material with a nanocrystalline starting structure. Interestingly, they found that there was no difference in mechanical wear between conventional and nanocrystalline microstructures, which was attributed to the negating effect of the thin carbonaceous tribofilm on the surface. The tribocorrosion aspects were complex, with the nanocrystalline surface promoting lower mechanical wear rates, but resulting in increased corrosion rates due to wear compared to the conventional structure, but a significantly reduced wear rate due to corrosion. The overall effect was that the nanocrystalline structure had a slightly lower wear rate than the conventional structure, which was entirely due to the dominant effect of the reduced wear rate due to corrosion.

5. Conclusions

1) The findings highlight the influence of environmental conditions on the tribocorrosion behaviour of the CoCrMo alloy under high-load testing conditions.
2) The open-air condition resulted in higher wear rates and rougher surfaces compared to the Ar condition.
3) The oxygen levels did not appreciably alter the friction.
4) The formation of tribo-layers with distinct compositions and microstructures was observed, with differences in thickness and uniformity between the two conditions. An oxide layer was present on the open-air tests but absent on the anaerobic Ar tests.
5) The strain accumulation was greater at the worn surface of the open-air condition than in the anaerobic Ar tests. In addition, the extent of friction-induced phase transformations from FCC to HCP phase was greater in the open-air condition, a result of higher surface strain. Given that the stress distribution would have been essentially the same in each case, the difference is associated with the role of oxides blocking dislocation annihilation.
6) The anaerobic tests exhibited all the same features, i.e. lower wear, less surface deformation and thinner tribofilm, compared to applying a cathodic polarisation to the sample. Thus, wear was predominantly mechanical with minimal wear accelerated corrosion.
7) The ratio of the Co, Cr and Mo content in the post test lubricant was different to the starting metal, with the Mo content much higher and the Cr content reduced. The metal content increased with load for the open-air tests, but remained constant as a function of load for the Ar tests. These results are consistent with the differences in the chemical wear contributions to the total wear between the two environments.

CRediT authorship contribution statement

J. Qi: Writing – original draft, Investigation, Formal analysis, Data curation, Conceptualization. **T. Cole:** Investigation. **A. Foster:** Investigation. **W.M. Rainforth:** Writing – review & editing, Supervision, Funding acquisition, Conceptualization.

Declaration of competing interest

The authors declare that they have no known competing financial interests or personal relationships that could have appeared to influence the work reported in this paper.

Data availability

Data will be made available on request.

Acknowledgement

This work is supported by the Engineering and Physical Sciences Research Council (grant number EP/001766/1) as a part of 'Friction: The Tribology Enigma' Programme Grant (www.friction.org.uk), a collaboration between the Universities of Leeds and Sheffield. The authors wish to acknowledge the Henry Royce Institute for Advanced Materials, funded through EPSRC grants EP/R00661X/1, EP/S019367/1, EP/P02470X/1 and EP/P025285/1, for access to the JEOL JEM-F200 and Bruker TriboLab through Royce@Sheffield.

References

[1] H. McKellop S-H Park, R. Chiesa, P. Doorn, B. Lu, P. Normand, P. Grigoris, H. Amstutz, In vivo wear of 3 Types of metal on metal hip prostheses during 2 Decades of Use, Clin. Orthop. Relat. Res. 329 (1996) s128–S140. Available: https://journals.lww.com/clinorthop/Fulltext/1996/08001/In_Vivo_Wear_of_3_Types_of_Metal_on_Metal_Hip.13.aspx.

[2] S.R. Brown, W.A. Davies, D.H. DeHeer, A.B. Swanson, Long-term survival of McKee-Farrar total hip prostheses, Clin. Orthop. Relat. Res. 402 (2002) 157–163, https://doi.org/10.1097/00003086-200209000-00013.

[3] H.J. Cooper, R.M. Urban, R.L. Wixson, R.M. Meneghini, J.J. Jacobs, Adverse local tissue reaction Arising from corrosion at the Femoral Neck-body Junction in a

Dual-Taper Stem with a cobalt-chromium Modular Neck, J. Bone Jt. Surgery-American 95 (2013) 865–872, https://doi.org/10.2106/JBJS.L.01042.
[4] W.M. Rainforth, P. Zeng, L. Ma, A.N. Valdez, T. Stewart, Dynamic surface microstructural changes during tribological contact that determine the wear behaviour of hip prostheses: metals and ceramics, Faraday Discuss 156 (2012) 41–57, https://doi.org/10.1039/c2fd00002d.
[5] R. Namus, P. Zeng, W.M. Rainforth, Correlation of the wear transition in CoCrMo alloys with the formation of a nanocrystalline surface layer and a proteinaceous surface film, Wear 376–377 (2017) 223–231, https://doi.org/10.1016/j.wear.2016.11.046.
[6] D. Sun, J.A. Wharton, R.J.K. Wood, Micro- and Nano-scale tribo-corrosion of cast CoCrMo, Tribol. Lett. 41 (3) (Mar. 2011) 525–533, https://doi.org/10.1007/s11249-011-9757-y.
[7] B. Thornley, R. Beadling, M. Bryant, A. Neville, Investigation of the repassivation process of CoCrMo in simulated Biological fluids, Corrosion 76 (6) (2020) 539–552, https://doi.org/10.5006/3423.
[8] T.P. Keeley, G.E. Mann, Defining physiological normoxia for improved translation of cell physiology to animal models and humans, Physiol. Rev. 99 (2019) 161–234, https://doi.org/10.1152/physrev.00041.2017.
[9] W.A. Brainard, D.H. Buckley, Preliminary friction a N D wear studies of cobalt-Rhenium solid solution in air and in vacuum [Online]. Available: https://core.ac.uk/download/pdf/80653476.pdf, 1971.
[10] D.H. Buckley, R.L. Johnson, Influence of crystal structure on friction characteristics of Rare-Earth and related metals in vacuum to 10 −10 mm of Mercury, ASLE Trans. 8 (1965) 123–132, https://doi.org/10.1080/05698196508972086.
[11] D.H. Buckley, R.L. Johnson, The influence of crystal structure and some properties of hexagonal metals on friction and adhesion, Wear 11 (1968) 405–419, https://doi.org/10.1016/0043-1648(68)90550-4.
[12] D.H. Buckley, T.J. Kuczkowski, R.L. Johnson, Influence of crystal structure on the friction and wear of titanium and titanium alloys in vacuum, Wear 9 (1966) 244, https://doi.org/10.1016/0043-1648(66)90206-7.
[13] C.-W. Cho, Y.-Z. Lee, Effects of oxide layer on the friction characteristics between TiN coated ball and steel disk in dry sliding, Wear 254 (2003) 383–390, https://doi.org/10.1016/S0043-1648(03)00021-8.
[14] J. Qi, G. Wang, W.M. Rainforth, Tribocorrosion Behaviour of CoCrMo in Simulated Body Fluid under Anaerobic Condition Part II: under Low Load, 2024 in preparation.
[15] F. Bachmann, R. Hielscher, H. Schaeben, Grain detection from 2d and 3d EBSD data—specification of the MTEX algorithm, Ultramicroscopy 111 (2011) 1720–1733, https://doi.org/10.1016/j.ultramic.2011.08.002.
[16] J. Qi, D. Guan, J. Nutter, B. Wang, W.M. Rainforth, Insights into tribofilm formation on Ti-6V-4Al in a bioactive environment: Correlation between surface modification and micro-mechanical properties, Acta Biomater. 141 (2022) 466–480, https://doi.org/10.1016/j.actbio.2022.01.027.
[17] Y. Xu, J. Qi, J. Nutter, J. Sharp, M. Bai, L. Ma, W.M. Rainforth, Correlation between the formation of tribofilm and repassivation in biomedical titanium alloys during tribocorrosion, Tribol. Int. 163 (2021) 107147, https://doi.org/10.1016/j.triboint.2021.107147.
[18] J. Qi, L. Ma, P. Gong, W.M. Rainforth, Investigation of the wear transition in CoCrMo alloys after heat treatment to produce an HCP structure, Wear 518 (2023) 204649, https://doi.org/10.1016/j.wear.2023.204649.
[19] J. Perret E. Boehm-Courjault, M. Cantoni, S. Mischler, A. Beaudouin, W. Chitty, J.-P. Vernot, EBSD, SEM and FIB characterisation of subsurface deformation during tribocorrosion of stainless steel in sulphuric acid, Wear 269 (2010) 383–393, https://doi.org/10.1016/j.wear.2010.04.023.
[20] M. Favero, P. Stadelmann, S. Mischler, Effect of the applied potential of the near surface microstructure of a 316L steel submitted to tribocorrosion in sulfuric acid, J. Phys. D Appl. Phys. 39 (2006) 3175–3183.
[21] A. Bidiville, M. Favero, P. Stadelmann, S. Mischler, Effect of surface chemistry on the mechanical response of metals in sliding tribocorrosion systems, Wear 263 (2007) 207–217.
[22] Cobalt Ions In Vivo, National Institute of Environmental Health Science, 111 TW Alexander Dr, Durham, NC 27709, Apr. 2016, https://doi.org/10.22427/ROC-MGRAPH-06.
[23] S. Wilbur, S. Wilbur, H. Abadin, M. Fay, D. Yu, B. Tencza, L. Ingerman, J. Klotzbach, S. James, Toxicological Profile for Chromium, Vi. Agency for Toxic Substances and Disease Registry (US), 2012 [Online]. Available: https://www.ncbi.nlm.nih.gov/books/NBK158859.
[24] T. Tyner, J. Francis, Molybdenum Trioxide, in: ACS Reagent Chemicals, American Chemical Society, Washington, DC, 2017, https://doi.org/10.1021/acsreagents.4231.20160601.
[25] T.A. Simoes, M.G. Bryant, A.P. Brown, S.J. Milne, M. Ryan, A. Neville, R. Brydson, Evidence for the dissolution of molybdenum during tribocorrosion of CoCrMo hip implants in the presence of serum protein, Acta Biomater. 45 (2016) 410–418, https://doi.org/10.1016/j.actbio.2016.08.051.
[26] R. Namus, W.M. Rainforth, Y. Huang, T.G. Langdon, Effect of grain size and crystallographic structure on the corrosion and tribocorrosion behaviour of a CoCrMo biomedical grade alloy in simulated body fluid, Wear (2020) 478–479, https://doi.org/10.1016/j.wear.2021.203884, 203884.